ASTFE
American Society
of Thermal and Fluids Engineers

10th Thermal and Fluids Engineering Conference (TFEC)
March 9-12, 2025
Partially Online Virtual and at George Washington University, Washington, DC Conference

TFEC-2025-56348

ADVANCED NUMERICAL MODELING OF OSWEC USING OPENFOAM AND OVERSET MESH STRATEGY

Minge Jiang* **and Danesh Tafti**

Mechanical Engineering Department, Virginia Tech, Blacksburg, VA 24061

ABSTRACT

Ocean wave energy has gained significant attention in the renewable energy sector, leading to the development and study of various wave energy converters (WECs). Among these, the Oscillating Surge Wave Energy Converter (OSWEC) has demonstrated a higher power capture width ratio (CWR) and easier operation and installation. While field tests provide valuable performance data, they are often costly and time-consuming. Numerical modeling offers a more efficient and cost-effective alternative. High-fidelity models, such as Computational Fluid Dynamics (CFD), offer more accurate predictions for realistic design needs. However, the complexity of coupling multiphase flow, wave dynamics, and six-degree-of-freedom rigid body motion presents challenges for high-fidelity CFD modeling in the WEC field. This research employs OpenFOAM, an open-source CFD software, utilizing the overset mesh strategy coupled with built-in wave models and a numerical wave tank (NWT) to simulate multiphase flow and rigid body dynamics of the OSWEC, and to investigate the hydrodynamic characteristics of the wave-structure interaction (WSI) system. The overset mesh strategy uses a fixed overset mesh attached to the rigid body to prevent errors caused by the grid deformation from dynamic mesh and reduce computational costs. The CFD model is validated against existing experimental and CFD results from the literature, yielding good agreement. Convergence tests demonstrate that a minimum cell per wave height (CPH) is necessary to reduce numerical noise. The overset mesh strategy is shown clearly advantageous for fluid-structure interaction (FSI). Future work will focus on utilizing this CFD model for the optimization of OSWEC design and Power Take Off (PTO) control systems.

KEY WORDS: Oscillating Surge Wave Energy Converter (OSWEC), Wave Energy Converters (WECs), Overset Mesh, OpenFOAM, Multiphase Flow, Numerical Wave Tank (NWT), Computational Fluid Dynamics (CFD), Fluid-Structure Interaction (FSI), Wave-Structure Interaction (WSI)

NOMENCLATURE

a	Wave amplitude	(m)	α	Volume fraction of a phase	(-)
F_x, F_y, F_z	Force x,y,z components	(N)	η	Free surface elevation	(m)
h	Water depth	(m)	θ_0	Initial phase	(rad)
H	Wave height	(m)	ν	Kinematic viscosity	(m^2/s)
k	Wave number	(-)	ϕ	Potential function	(-)
M_x, M_y, M_z	Moment x,y,z components	(Nm)	ω	Wave angular frequency	(rad/s)
U_x, U_y, U_z	Velocity x,y,z components	(m/s)	Ω_x, Ω_y, Ω_z	Vorticity x, y, z component	(1/s)

*Corresponding Author: mingej@vt.edu

1. INTRODUCTION

Ocean wave energy represents a substantial untapped resource, with its annual technical potential estimated to be about one-third of the U.S. yearly electricity generation [1]. This immense potential has driven the development of various wave energy converters (WECs), particularly over the past two decades. WECs are typically categorized by their operating principle into oscillating water column, oscillating bodies, and overtopping devices [2], or based on directional dependency, which divides into point absorber, attenuator, and terminator [3]. Among these, the oscillating bodies, such as bottom-hinged oscillating surge wave energy converters (OSWEC), are noted for having the highest power capture width ratio (CWR) [4].

The full-scale field studies of these devices provide valuable data under real-world conditions, but they are often expensive, highly site-specific, and limited to testing specific devices [5]. Laboratory-scale tests while more cost-effective and conducted under controlled wave conditions, are constrained by the physical limitations of wave flumes and equipment [6], [7]. In contrast, numerical modeling offers greater flexibility, allowing researchers to simulate a broad range of wave conditions and design parameters for various WEC configurations. Compared to low-fidelity models, which have lower computational costs and accuracy, high-fidelity computational fluid dynamics (CFD) can simulate WEC models with the flexibility of numerical modeling and high accuracy [8], [9].

OpenFOAM, a widely used open-source CFD software, is frequently applied to solve problems involving incompressible and compressible fluids, heat transfer, turbulence, and rigid body dynamic, and more [10]. In the literature, OpenFOAM is used in over 35% of high-fidelity wave energy modelling studies [11], [12], making it the most commonly utilized CFD software among all available commercial codes due to its versatility and open-source accessibility. The newly integrated solver, *overInterDyMFoam*, specifically handles six-degree-of-freedom rigid body motion using a more efficient mesh strategy known as Overset Mesh. First introduced in the 1990s, the overset mesh technique has evolved to facilitate two-way coupled rigid body motion in CFD simulations [13]. Traditional dynamic meshing and remeshing strategies often require either non-orthogonal grids, cell deformation, and limitations of body movement, or frequently remeshing that increases computational costs. On contrary, the overset mesh approach uses a local mesh that is attached to the body overlapping with the background grid, allowing for simpler grid generation and reduced computational costs while preventing mesh deformation [14]. Due to the complexity of coupling OpenFOAM multiphase flow, wave dynamics, constrained rigid body motion of the OSWEC, and overset mesh, such models are only seen in a few literature [15], [16].

Common numerical wave generation techniques in the CFD numerical wave tank (NWT) include the relaxation method (RZM), static boundary method (SBM), and dynamic boundary method (DBM) [17]. Unlike the relaxation method, which typically requires additional inlet and outlet zones to introduce and absorb waves, the static boundary method directly imposes the theoretical wave as a boundary condition at the inlet patch, saving computational domain space and reducing computational costs. OpenFOAM's build-in utility, *wavemodels*, employs the SBM to generate waves, making it the preferred choice for this study.

This research aims to establish a reliable OSWEC model by couple the *overInterDyMFoam* solver from OpenFOAM v2312, with build-in *wavemodels*. The model is tested against literature CFD and experimental data for validation. The convergence tests are evaluated with several different grid levels to investigate the impacts of grid resolution for accuracy and computational efficiency of this model, and provide reference for future applications, which will focus on applying this model for optimization of OSWEC design and power take-off (PTO) control systems.

2. METHODOLOGY

The governing equations for fluid dynamics are the Navier-Stokes equations for conservation of mass and momentum.

$$\nabla \cdot \left(\rho \vec{U}\right) = 0 \tag{1}$$

$$\frac{\partial U}{\partial t} + \nabla \cdot \left(\vec{U}\vec{U}\right) = -\frac{1}{\rho}\nabla p + \nabla \cdot \left(\nu \nabla \vec{U}\right) \tag{2}$$

The solver *overInterDyMFoam* in OpenFOAM handles two phase incompressible, immiscible fluids, coupled with dynamic and overset meshing techniques. It applies the Volume of Fluid (VOF) method to capture the sharp interface between the two phases and uses the *sixDoFRigidBodyMotion* library to simulate constrained rigid body dynamics. For VOF method, the fluid properties are initially defined by a volume fraction α of the phase within a cell. The interphase equation is then solved to obtain α. For density ρ:

$$\rho = \alpha\rho_1 + (1-\alpha)\rho_2 \tag{3}$$

$$\frac{\partial \alpha}{\partial t} + \nabla \cdot \left(\vec{U}\alpha\right) = 0 \tag{4}$$

The discretization schemes incorporate explicit Euler for time derivatives, Gauss Linear for gradients, and Gauss Upwind for divergence terms. The numerical algorithm PIMPLE is used to efficiently solve the transient pressure-velocity coupling in the incompressible Navier-Stokes equations. For overset interpolation between the overset and background meshes, the *cellVolumeWeight* method is utilized. In OpenFOAM versions prior to v2212, fluid data transfer between meshes used a single layer of cells directly adjacent to the rigid body. However, the updated overset interpolation algorithm now allows users to adjust the interpolation layer for improved accuracy. In this study, 4-6 layers from the flap surface were used, with the layer 3 selected for interpolation. Only laminar flow is considered for the purpose of this study.

The theoretical wave solution is generated at the inlet using the Static Boundary Method (SBM) wavemaker in the numerical wave tank (NWT), while *shallowWaterAbsorption* is applied at the outlet to absorb the waves. The tested wave is a regular Stokes first-order wave characterized by a height of 0.038 m, period 2.063 s, speed 2.039 m/s, and wavelength 4.21 m. Using potential flow theory and linearized small wave assumptions, along with the appropriate boundary conditions, the dispersion relation and the theoretical solution of the Stokes first-order wave can be derived. For a 2-D wave, the solutions are presented below.

$$w^2 = gk\, tanh(kh) \tag{5}$$

$$\emptyset = -\frac{ga}{w}\frac{cosh(ky+kh)}{cosh(kh)}sin(kx - wt + \theta_0) \tag{6}$$

$$u = -\frac{\partial\emptyset}{\partial x} = \frac{gak}{w}\frac{cosh(ky+kh)}{cosh(kh)}cos(kx - wt) \tag{7}$$

$$v = -\frac{\partial\emptyset}{\partial y} = \frac{gak}{w}\frac{sinh(ky+kh)}{cosh(kh)}sin(kx - wt) \tag{8}$$

The wave propagates along the x-axis, with the z-axis defined as the vertical direction. The *waveVelocity* boundary condition is applied to the inlet and outlet patches, the top boundary is set as *pressureInletOutletVelocity*, and the bottom boundary condition is *noSlip*. Symmetry condition is applied at the front and back boundaries.

The domain geometry follows the setup used in Munoz's Thesis [15] with adjustments, and has dimensions of 20 m (x-axis) x 1.8 m (y-axis) x 1 m (z-axis), with a water depth of 0.5 m. The flap geometry is rectangular, measuring 0.1 m (thickness) x 0.65 m (width) x 0.34 m (height), with 0.1 m extending above the water surface. The flap is hinged along the y-axis, positioned 0.02 m above its base, with the hinge located 0.28 m above the bottom of the domain. The background grid is first generated using the *blockMesh* method for structured orthogonal meshes, followed by a refined zone is applied along the wave interface area and around the flap, with a refinement ratio of 1. Total seven background grid levels were tested for convergence. The cells per wavelength (CPW) range from 168 to 421 in the refined zone, while the cells per wave height (CPH) range from 4 to 16. The total cell number of the domain begins from 1.67 million and increases to 37.9 million.

The overset mesh is generated 0.1 m to 0.15 m from the flap surface, with a slightly finer mesh size compared to the background. For testing purpose, only two overset grid levels were employed in all cases. The flap and the overset mesh, are centered along both the x- and y-axes in the domain. The surface features are first extracted from the flap geometry file, after which the *snappyHexMesh* utility is used to generate mesh around the flap, with a refined zone applied near the surface. Additional testing parameters and detailed grid levels are provided in **Table 1**. To account for the experimental hinge bearing friction, a damping coefficient of 1.0 Ns/m was used for validation purposes.

Table 1 Convergence tests case grid resolution summary table.

Case	Refined Background Zone				Refined Overset Zone		Total Cell Num (Million)
	dx, dy (m)	dz (m)	CPW	CPH	dx, dy (m)	dz (m)	
G1	0.025	0.0095	168	4	0.01	0.005	1.67
G2	0.025	0.0063	168	6			2.4
G3	0.02	0.00475	210	8			4.98
G4	0.0175	0.003165	240	12			9.4
G5	0.015	0.002375	280	16	0.00625	0.0025	17.3
G6	0.0125	0.0027	336	14			21.7
G7	0.01	0.002375	421	16			37.9

The angular velocity and the rotation angle of the flap tip center, along with the total hydrodynamic forces and moments acting on the flap about the center of rotation, were compared. A median filter is applied to the force and moment data for enhanced visualization. To obtain the free surface elevation η, the volume ratio α was sampled at the center of the y-axis, and at various locations along the x-axis, then integrated vertically for examination and comparison.

$$\eta = \int_{Bottom}^{Top} \alpha \, dz \tag{9}$$

The results were phase-shifted for comparison due to differences in domain setup, position and sampling locations between the literature and the test cases. Tangential acceleration was calculated and compared using formulas from the referenced paper [15].

3. RESULTS AND DISCUSSION

The domain and mesh diagram, along with selected 2D slices of the hydrodynamic fields are shown in **Fig. 1** and **Fig. 2**. The corresponding results are presented in **Fig. 4** to **Fig. 9**.

The sampled free surface elevation (FSE) at various locations is illustrated in **Fig. 3** and compared to experimental data from [18] in **Fig. 4**. The FSE results align well with the theoretical Stokes first-order wave solution in terms of wave height and period. Case G1, and G7 exhibit slightly larger wave height compared to all other cases. The generated wave is shifted downward by approximately 0.002 m compared to the theoretical solution. This finding is consistent with experimental data [18], showing that the wave troughs are deeper than the wave crests and represents an improvement over their numerical results obtained using arbitrary mesh interface (AMI). As the sampling location moves closer to the flap, the wave experiences increased reflection from the structure, resulting in a rise in wave height, as seen in **Fig. 3**, and a distorted shape in **Fig. 4**. The

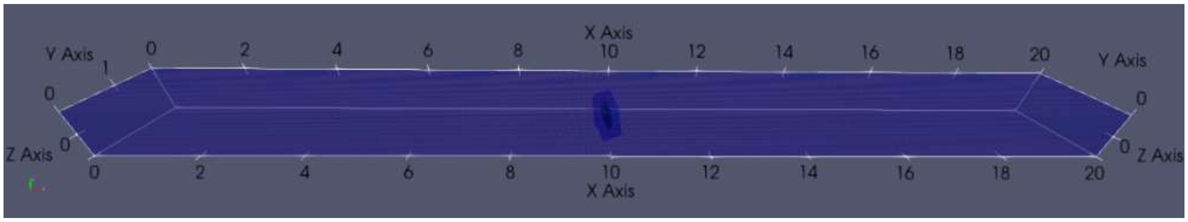

a. 3D domain with flap

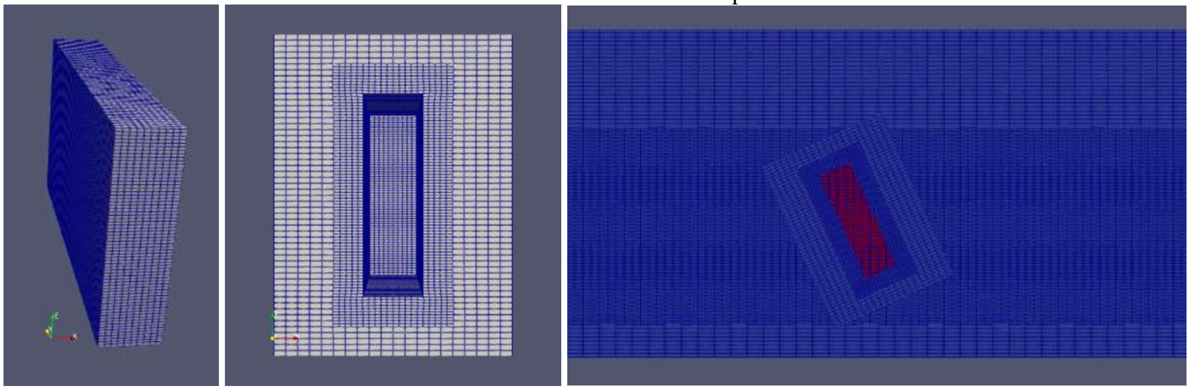

b. 3D Flap mesh c. 3D Front view, overset mesh d. 2D Background + overset mesh

Fig. 1 Overview of the computational model setup: a. Model 3D domain; b. 3D flap mesh; c. 3D Front view of the overset mesh with the flap at the center of y-axis; d. Background plus overset mesh 2D front center slice.

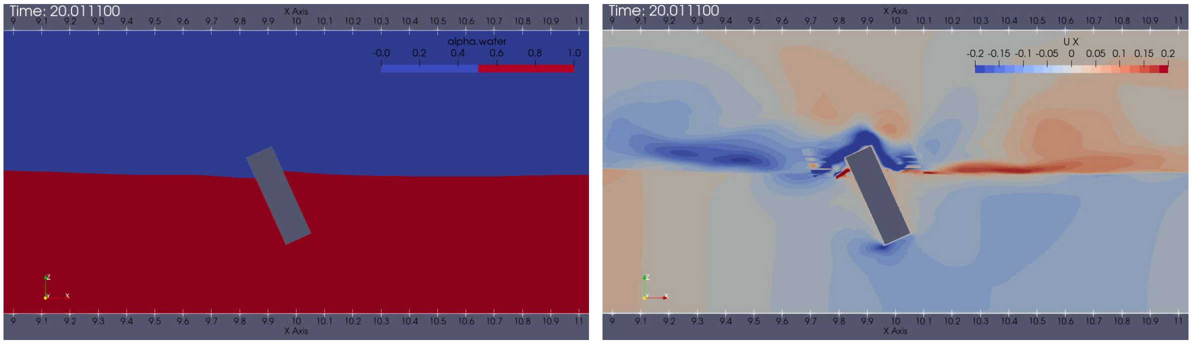

a. 2D Front center slice, phase b. 2D Front center slice, U_x

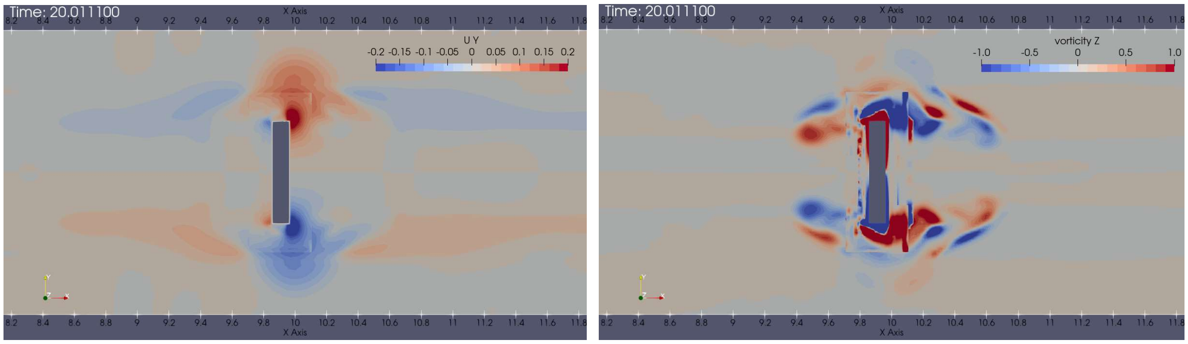

c. 2D Top center slice at z=-0.02m, U_y d. 2D Top center slice, Ω_z

Fig. 2 Fluid hydrodynamic field characteristics: a. 2D Front center slice at y = 0.9 m, phase; b. 2D Front center slice at y = 0.9 m, *Ux*; c. 2D Top center slice at z = -0.02 m, *Uy*; d. 2D Top center slice at z = -0.02 m, vorticity Ω_z.

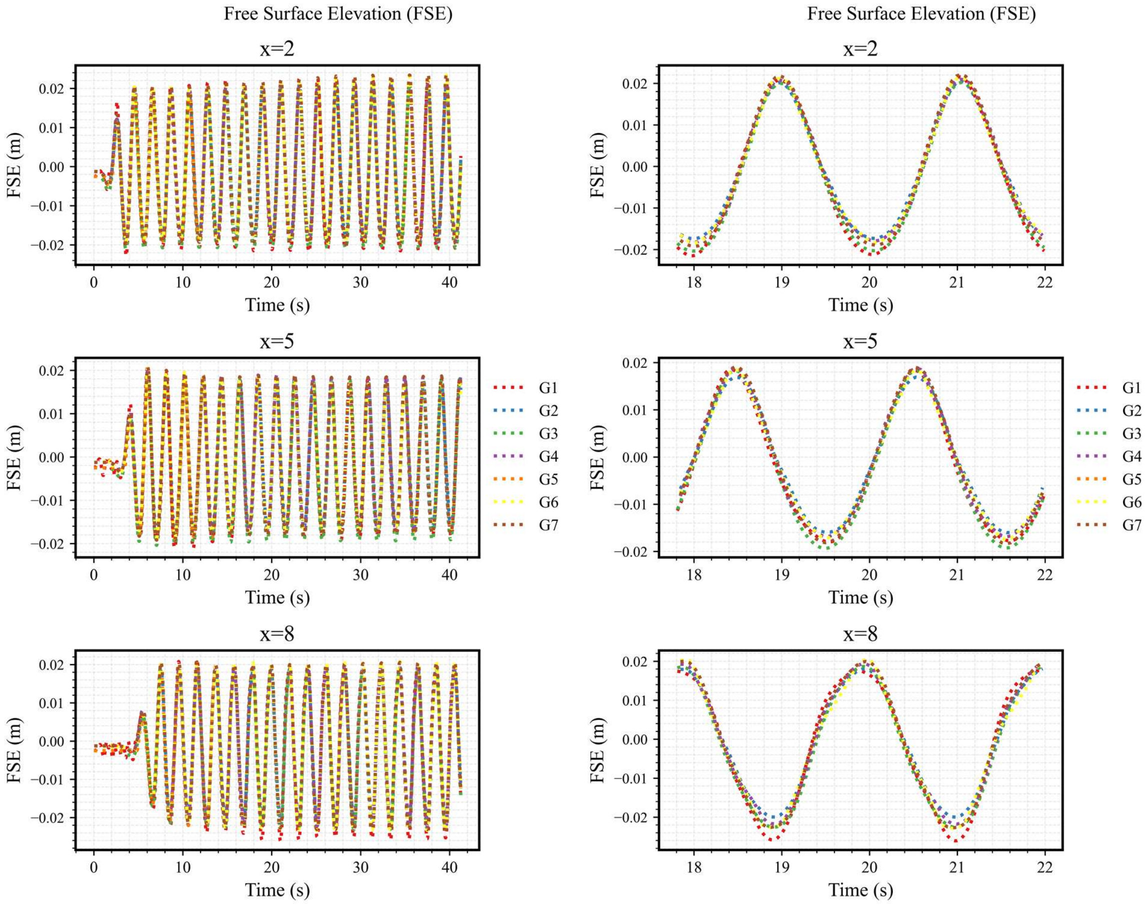

a. FSE at various locations

b. FSE at various locations for two wave periods

Fig. 3 Free surface elevation sampling at x=2 m, 5 m and 8 m: a. FSE sampling with time; b. FSE sampling for two wave periods.

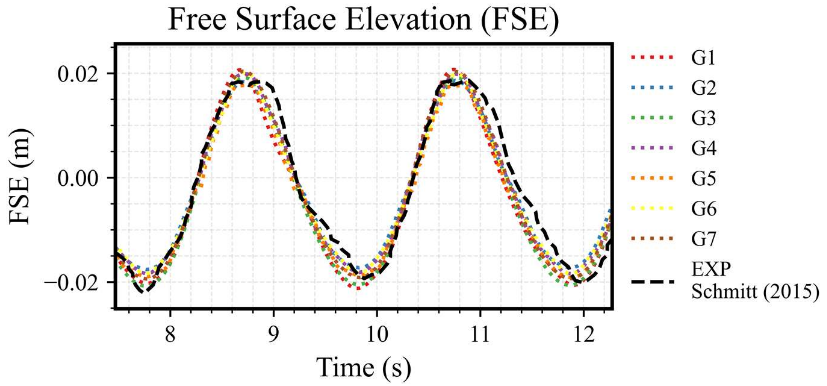

Fig. 4 Free Surface Elevation sampling at x = 2 m, compared with experimental data.

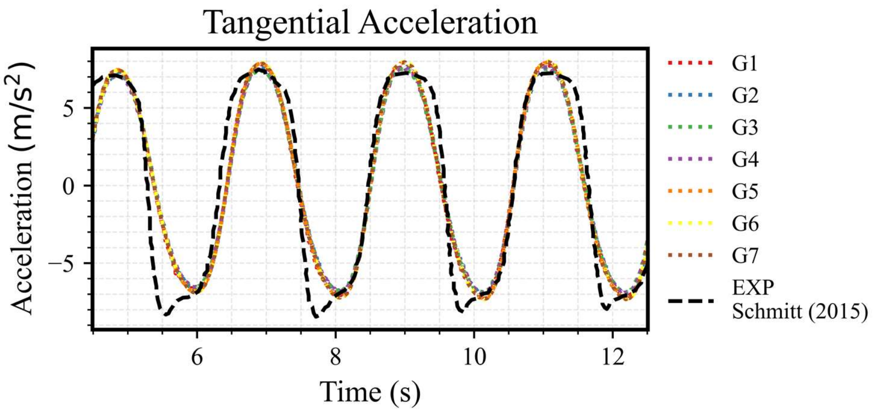

Fig. 5 Tangential Acceleration (m/s^2) compared with experimental data.

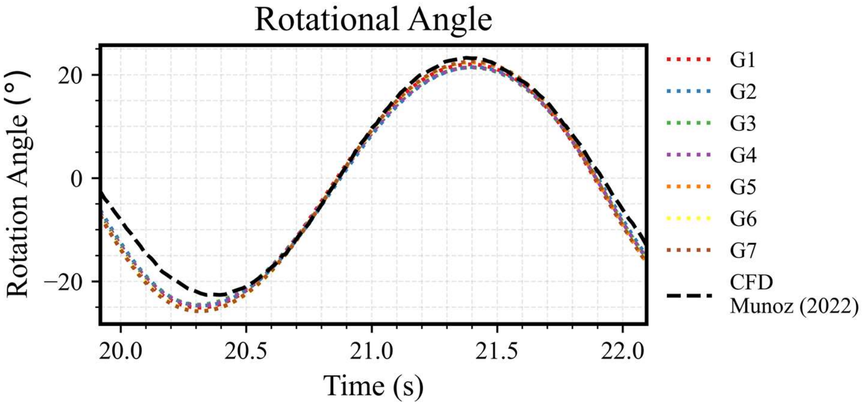

a. Rotation Angle

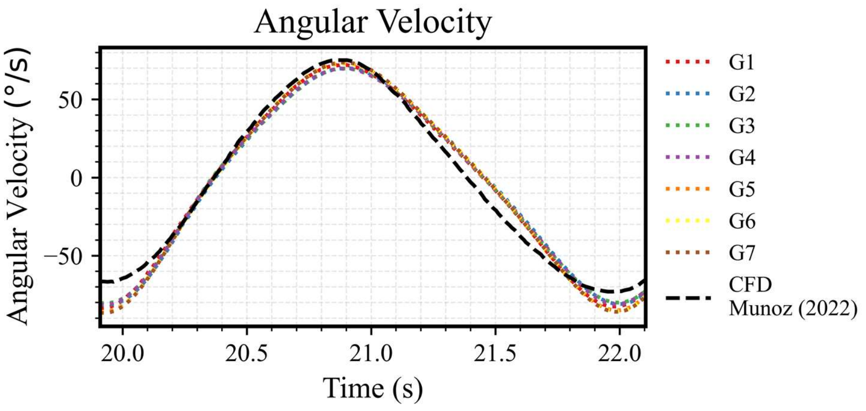

b. Angular Velocity

Fig. 6 Rotation angle and Angular velocity at the top center of the flap, compared with literature CFD data: a. Rotation angle (◦); b. Angular velocity (◦/s).

wave sampled at x = 8 m shows clear nonlinearity compared to the sampling at x = 2 m. **Fig. 3** demonstrates stable wave generation over 20 wave periods, confirming the stability of the model.

The tangential acceleration at the top center of the flap about the center of rotation, is calculated based on hydrodynamic force and moment acting on the body, and compared in **Fig. 5**. It shows good agreement with the experimental data, with minor deviations near the wave valley due to differences in domain setup. Specifically, the numerical domain was flattened following the model used by Munoz [15], while the experimental wave tank featured contoured bottom. This differences likely caused the observed variations near the wave valley, as the simplified flat bottom alters wave dynamics compared to the experimental conditions. The rotation angle and angular velocity at the top center of the flap are presented in **Fig. 6**. The simulation results agree well with the literature CFD data [19], and the differences between cases are minimal. However, the simulated negative and positive values are slightly moved downward by approximately 3 degrees, which is consistent with the downward shift observed in the free surface elevation. This phenomenon has a negligible influence on power extraction. The model results also exhibit a noticeable asymmetry in both the rotation angle and angular velocity, a feature not clearly reflected in the literature data.

Fig. 7 and **Fig. 8** present the total hydrodynamic forces and moments, as well as the forces and moments due to viscosity acting on the flap about its center of rotation. The variation in the x-component total force F_x is related to wave interaction, while the z-component total force, F_z, is dominated by hydrostatic forces. Since the flap is hinged about y-axis, the F_y value should theoretically be close to zero. As shown in the plot, all cases, except for G1, which exhibits relatively higher noise, have negligible F_y values, as expected. The reduction in noise from G1 to G2 can be attributed to an increase of two CPH in the z-axis grid resolution. Similar trends are observed in the total moment data. The y-component moment, M_y, responsible for the flap's rotation about y-axis, shows strong consistency across all cases. For M_x and M_z, aside from relatively higher noise in case G1, all other cases show trivial values. The noise in the total force and moment is several orders of magnitude smaller than the components of interest and thus negligible. Similarly, the viscous forces and moments are significantly smaller compared to the total forces and moments, indicating that the forces acting on the structure are predominantly due to pressure forces, thus justifying neglecting the effect of turbulent viscosity on the flap motion.

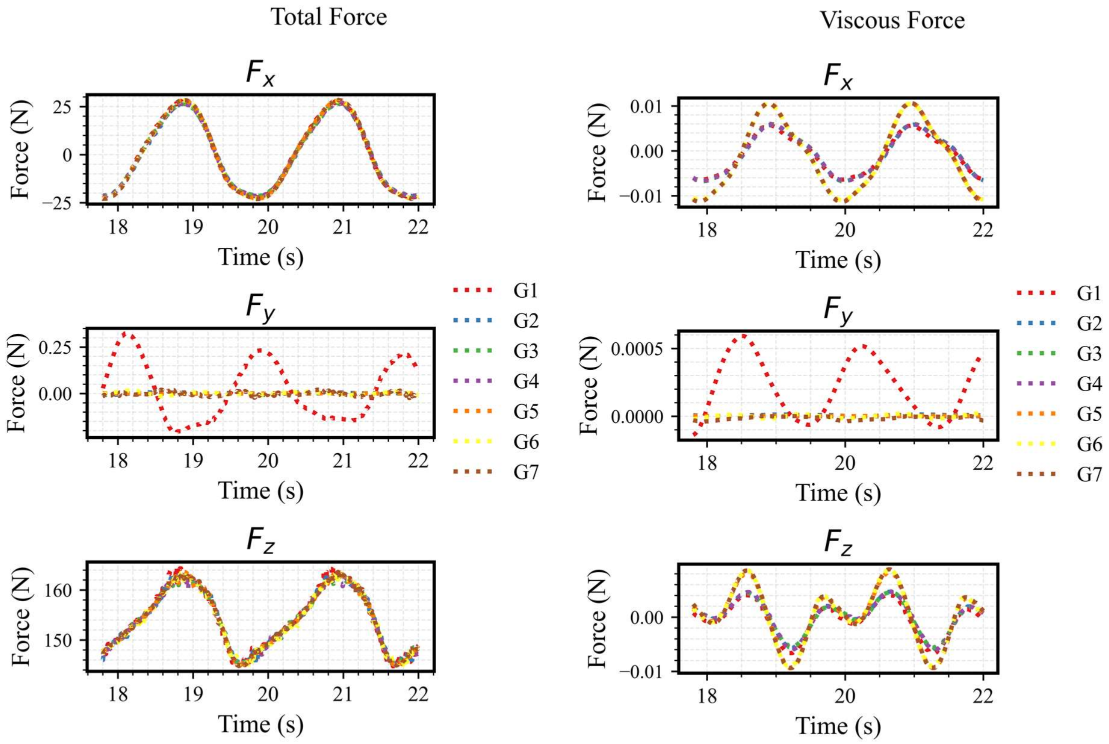

a. Total Force

b. Viscous Force

Fig. 7 Total force and viscous force at x, y, and z-axis acting on the flap about the center of rotation for two wave periods: a. Total Force (N); b. Viscous force (N).

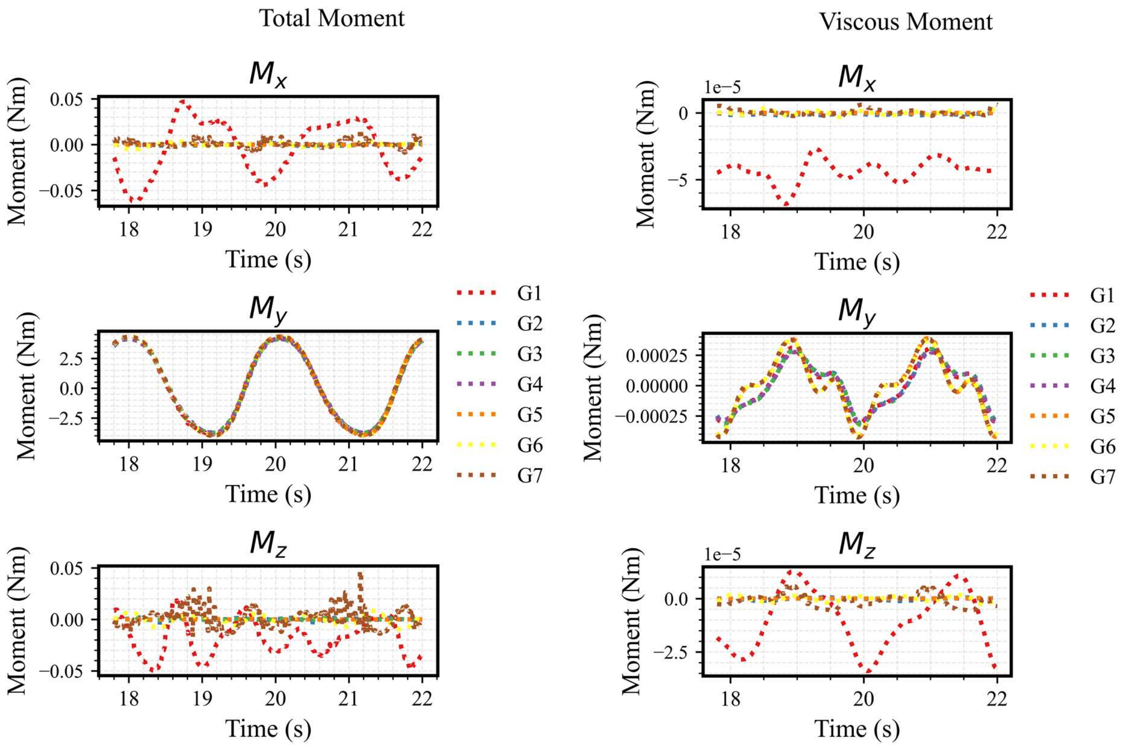

a. Total Moment

b. Viscous Moment

Fig. 8 Total Moment and viscous Moment at x, y, and z-axis acting on the flap about the center of rotation: a. Total Moment (Nm); b. Viscous Moment (Nm).

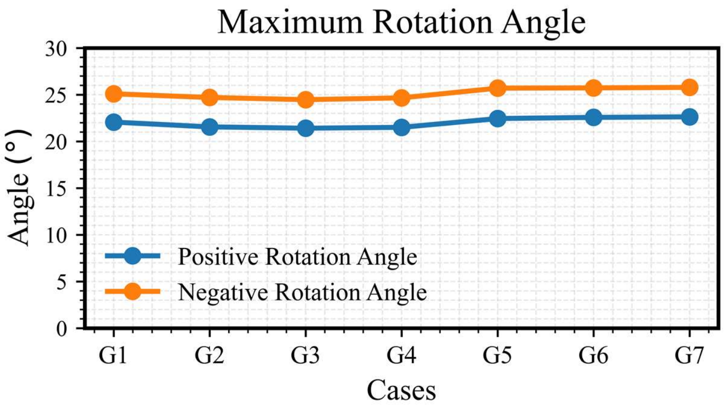

Fig. 9 Maximum rotation angle of the tip center of the flap comparison across cases.

Fig. 9 compares the maximum positive and negative rotation angle of the flap tip center compared across all cases. Within the overset grid level 1, the maximum rotation angle shows convergence from background mesh level G2 to G4. For overset grid level 2, the maximum rotation angles are nearly identical from G5 to G7, regardless of the background mesh levels. Moving from overset grid level 1 to level 2, there is an approximately 1-degree increase in the maximum rotation angle. However, for the same overset grid resolution, the differences are negligible. This indicates that the overset mesh resolution primarily influences the flap movement, which aligns with the expected behavior of the overset mesh. The asymmetrical rotation is clearly demonstrated in all cases by the difference between the positive and negative maximum rotation angles, which shows an increase of approximately 3 to 3.5 degrees from the positive to the negative maximum rotation angle. This effect likely results from the fact that the incoming wave is modified due to non-linear interactions with reflections from the flap. This is consistent with the FSE sampling data, which shows deeper troughs. Overall, the variations in the maximum rotation angle across cases are minor.

4. CONCLUSIONS

The OpenFOAM model, which couples two-phase incompressible flow with an Oscillating Surge Wave Energy Converter (OSWEC) interacting with waves, has been developed and validated against existing CFD and experimental data. The differences in data between cases are minimal; however, CPH is more critical than CPW regarding generated wave accuracy and model stability. The overset mesh offers clear advantages for fluid structure interaction. Additionally, the overset mesh resolution influences flap movement. Excluding the coarsest grid, all other grid levels with CPH equal to or greater than six demonstrate consistent data and align well with literature results. To achieve high accuracy while minimizing computational costs, it is recommended that the G2 and G3 levels of background grid, along with level 2 overset grid resolution, be utilized for future research. Viscous forces have been shown to be negligible in this model, with hydrodynamic forces predominantly driven by pressure forces. The model has demonstrated reliability in simulating the interaction between waves and the OSWEC, making it suitable for future research and design applications. Future work will focus on evaluating the effect of turbulence models, coupling various wave conditions, and optimizing the Power Take-Off (PTO) control system and design parameters.

ACKNOWLEDGMENT

The authors acknowledge support from the National Science Foundation, award number CMMI 2152694. The authors also acknowledge computing resources provided by Advanced Research Computing (ARC) at Virginia Tech.

REFERENCES

[1] L. Kilcher, M. Fogarty, and M. Lawson, (2021) “Marine Energy in the United States: An Overview of Opportunities,” NREL/TP--5700-78773, 1766861, MainId:32690, Feb. 2021. doi: 10.2172/1766861.

[2] W. Sheng, (2019) “Wave energy conversion and hydrodynamics modelling technologies: A review,” *Renewable and Sustainable Energy Reviews*, vol. 109, pp. 482–498, Jul. 2019, doi: 10.1016/j.rser.2019.04.030.

[3] I. López, J. Andreu, S. Ceballos, I. M. De Alegría, and I. Kortabarria, (2013) “Review of wave energy technologies and the necessary power-equipment,” *Renewable and sustainable energy reviews*, vol. 27, pp. 413–434, 2013.

[4] T. Aderinto and H. Li, (2019) “Review on Power Performance and Efficiency of Wave Energy Converters,” *Energies*, vol. 12, no. 22, p. 4329, Nov. 2019, doi: 10.3390/en12224329.

[5] T. Whittaker and M. Folley, (2012) “Nearshore oscillating wave surge converters and the development of Oyster,” *Phil. Trans. R. Soc. A.*, vol. 370, no. 1959, pp. 345–364, Jan. 2012, doi: 10.1098/rsta.2011.0152.

[6] M. Brito, R. M. L. Ferreira, L. Teixeira, M. G. Neves, and R. B. Canelas, (2020) “Experimental investigation on the power capture of an oscillating wave surge converter in unidirectional waves,” *Renewable Energy*, vol. 151, pp. 975–992, May 2020, doi: 10.1016/j.renene.2019.11.094.

[7] A. Henry, O. Kimmoun, J. Nicholson, G. Dupont, Y. Wei, and F. Dias, (2014) “A two dimensional experimental investigation of slamming of an oscillating wave surge converter,” in *ISOPE International Ocean and Polar Engineering Conference*, ISOPE, 2014, p. ISOPE-I. Accessed: Oct. 11, 2024. [Online]. Available: https://onepetro.org/ISOPEIOPEC/proceedings-abstract/ISOPE14/All-ISOPE14/14246

[8] A. Ahmed *et al.*, (2024) “Performance characterization and modeling of an oscillating surge wave energy converter,” *Nonlinear Dyn*, vol. 112, no. 6, pp. 4007–4025, Mar. 2024, doi: 10.1007/s11071-023-09248-2.

[9] P. Schmitt, (2013) “Investigation of the near flow field of bottom hinged flap type wave energy converters,” PhD Thesis, The Queen’s University of Belfast, 2013. doi: 10.13140/RG.2.1.1296.7921.

[10] C. Greenshields, (2024) “OpenFOAM v11 User Guide,” CFD Direct. Accessed: Apr. 28, 2024. [Online]. Available: https://doc.cfd.direct/openfoam/user-guide-v11/index/

[11] L. Huang *et al.*, (2022) “A Review on the Modelling of Wave-Structure Interactions Based on OpenFOAM,” *OpenFOAM J*, vol. 2, pp. 116–142, Aug. 2022, doi: 10.51560/ofj.v2.65.

[12] C. Windt, J. Davidson, and J. V. Ringwood, (2018) “High-fidelity Numerical Modelling of Ocean Wave Energy Systems: A Review of Computational Fluid Dynamics-Based Numerical Wave Tanks,” *Renewable and Sustainable Energy Reviews*, vol. 93, pp. 610–630, Oct. 2018, doi: 10.1016/j.rser.2018.05.020.

[13] M. Galbraith, P. Orkwis, and J. Benek, (2011) "Extending the Discontinuous Galerkin Scheme to the Chimera Overset Method," in *20th AIAA Computational Fluid Dynamics Conference*, Honolulu, Hawaii: American Institute of Aeronautics and Astronautics, Jun. 2011. doi: 10.2514/6.2011-3409.
[14] M. Alletto, (2022) "Comparison of overset mesh with morphing mesh: flow over a forced oscillating and freely oscillating 2D cylinder," *OpenFOAM® Journal*, vol. 2, pp. 13–30, 2022.
[15] D. Benites-Munoz, L. Huang, E. Anderlini, J. R. Marín-Lopez, and G. Thomas, (2020) "Hydrodynamic modelling of an oscillating wave surge converter including power take-off," *Journal of Marine Science and Engineering*, vol. 8, no. 10, p. 771, 2020.
[16] M. Riddle, (2022) "CFD Modeling of an Oscillating Wave Surge Converter using the Overset Grid Method," Master Thesis, University of Washington, 2022.
[17] A. Miquel, A. Kamath, M. Alagan Chella, R. Archetti, and H. Bihs, (2018) "Analysis of Different Methods for Wave Generation and Absorption in a CFD-Based Numerical Wave Tank," *JMSE*, vol. 6, no. 2, p. 73, Jun. 2018, doi: 10.3390/jmse6020073.
[18] P. Schmitt and B. Elsaesser, (2015) "On the use of OpenFOAM to model oscillating wave surge converters," *Ocean Engineering*, vol. 108, pp. 98–104, 2015.
[19] D. A. B. Munoz, (2022) "Numerical modelling of oscillating wave surge converters operating in array configurations," PhD Thesis, University College London, 2022.